arTs Università degli Studi di Trieste
Archivio della ricerca – postprint

Computationally Efficient Thermal Analysis of a Low-Speed High-Thrust Linear Electric Actuator With a Three-Dimensional Thermal Network Approach

Alberto Tessarolo, *Member, IEEE*, and Claudio Bruzzese, *Member, IEEE*

***Abstract*—Permanent-magnet synchronous linear motors (PMSLMs) are more and more frequently used as all-electric direct-drive actuators in those applications where a force needs to be developed along a fixed direction. In this paper, an accurate 3-D thermal model of a PMSLM is derived through a lumped-parameter network approach which exploits all the symmetries in the actuator structure to maximize the spatial density of nodes. Numerically efficient techniques are then proposed to solve the thermal network analytically. Some experimental validations are finally presented based on the thermal testing of a laboratory prototype.**

***Index Terms*—Linear actuators, lumped-parameter model, permanent-magnet synchronous machines, thermal analysis.**

I. Introduction

A LARGE variety of applications, spanning from industrial to household appliance fields, require that a force is applied along a fixed linear direction [1]. Permanent-magnet linear electric actuators are being more and more employed in such applications [2]–[11] as they exhibit several strengths compared to more traditional solutions [12], [13], with their main advantages being good efficiency, high reliability, and the suitability for a direct-drive coupling to the load.

As in the case of rotating machinery, a crucial task in the design of a permanent-magnet synchronous linear motor (PMSLM) is the prediction of its thermal behavior under given continuous or intermittent-load operating conditions [2], [3], [14], [15]. When the PMSLM is cooled by natural convection [2], [3], [14], [15] and/or is designed for fast-dynamics applications [2], [7], [8], its thermal study involves similar challenges to those encountered with rotating machines, such as determining the pressure, velocity, and temperature field of the cooling fluid and accounting for motion effects [16]–[20]. This can be typically done by such approaches as 3-D FEA modeling [19], [20] and an appropriate tuning of thermal lumped-parameter models through heuristic correction coefficients [16]–[18]. For instance, a FEA method is used in [3] and [15] for the accurate thermal simulation of PMSLMs, and measurements on a PMSLM prototype are used to calibrate thermal models in [2] and [15] in terms of heat transfer coefficients.

In the PMSLM design addressed in this paper [9]–[11], a genetic-optimization iterative process was adopted [10], which required running thousands of thermal simulations (one for each design explored). This made practically impossible to use a FEA simulation approach [19], [20] due to excessive computation times. Furthermore, there was no previously built similar equipment to be used as a reference for model tuning by experiments [2], [15]. Hence, the need arouse to develop a lumped-parameter algorithm for thermal analysis matching the following requirements: sufficient accuracy, very fast computation times, and no need for heuristic or measurement-based model calibration. The task was made feasible by a couple of peculiarities of the machine under study, i.e., the extremely slow mover speed and supply frequency (the actuator acts a slow-dynamics positioning system for high-thrust and highly inertial loads like ship rudders and bow thrusters [9], [11]), which allowed for core loss and motion effects [2], [14], [15] to be disregarded; the cooling of the machine was based on a forced water flow through a cold plate, and hence, natural convection, although present, played a minor effect [16], [17].

Owing to the mentioned simplifications, a lumped-parameter analytical method is developed to model the PMSLM by means of a 3-D equivalent thermal network [18] with the lowest possible number of nodes. To achieve a high level of detail with a limited node count, all the symmetries of the actuator structure are fully exploited which enable to significantly increase the spatial density of nodes.

The problem of a numerically efficient solution of the resulting thermal network is then addressed by means of appropriate analytical techniques based on matrix eigenvalue decomposition. By applying Laplace transforms and Fourier series expansions, analytical formulations are derived, giving a practically instantaneous solution of the PMSLM thermal model during stepwise load transients and in steady-state operation under intermittent loading.

Finally, the accuracy of the methodologies proposed is experimentally assessed based on the thermal testing of a laboratory prototype.

Manuscript accepted June 13, 2014.

A. Tessarolo is with the Department of Engineering and Architecture, University of Trieste, 34127 Trieste, Italy (e-mail: atessarolo@units.it).

C. Bruzzese is with the Department of Astronautical, Electrical and Energy Engineering, University of Rome "La Sapienza," 00185 Rome, Italy (e-mail: claudio.bruzzese@uniroma1.it).

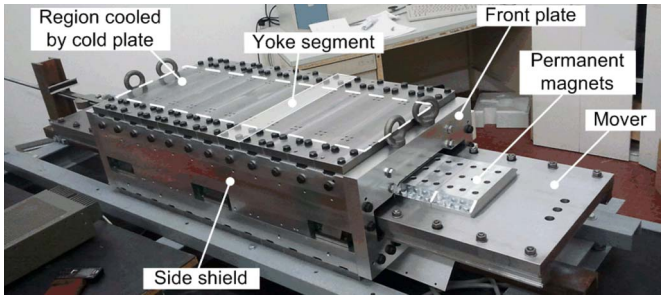

Fig. 1. Outside view of the PMSLM. The dashed rectangle indicates the area on which the cold plate is mounted.

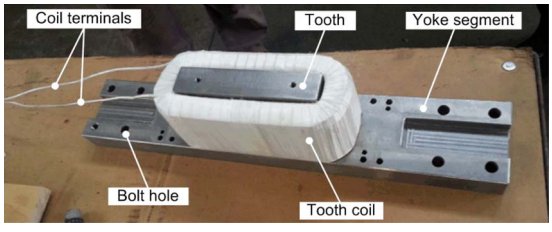

Fig. 2. Detail of yoke segment and tooth assembly with relevant tooth coil.

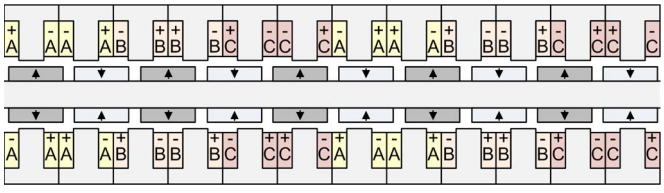

Fig. 3. PMSLM three-phase arrangements.

II. PMSLM General Description

The PMSLM considered in this paper is a linear electric actuator prototype specifically developed to potentially replace hydrostatic drives that are presently used to actuate very-low-speed and high-thrust shipboard loads such as rudders, stabilizing fins, bow thrusters, etc.[9]–[11]. The prototype structure, shown in Fig. 1, is very simple. It includes a solid-steel permanent-magnet mover sliding axially on linear bearings mounted along two aluminum side shields, which serve only a structural function. Permanent magnets are fixed to the mover by means of aluminum retention boxes. The stator active part consists of a sequence of identical wound teeth, each assembled to its relevant yoke section, as shown in Fig. 2. Yoke segments are, in turn, bolted to the aluminum side shields, 12 on the top half of the actuator (above the mover) and 12 on the bottom half (below the mover). Aluminum front plates are finally added at both actuator ends for mechanical strengthening purposes. A PMLSM axial section is shown in Fig. 3 showing how the tooth coils are assigned to phases for winding supply: It can be seen that a fractional-slot concentrated-winding design featuring 12 slots and ten poles is adopted [21].

A schematic representation of the PMSLM, with some significant dimensions, is represented in Fig. 4 (coils and front plates are omitted for clarity's sake). Here, the three Cartesian axes are denoted with letters l (length), h (height), and

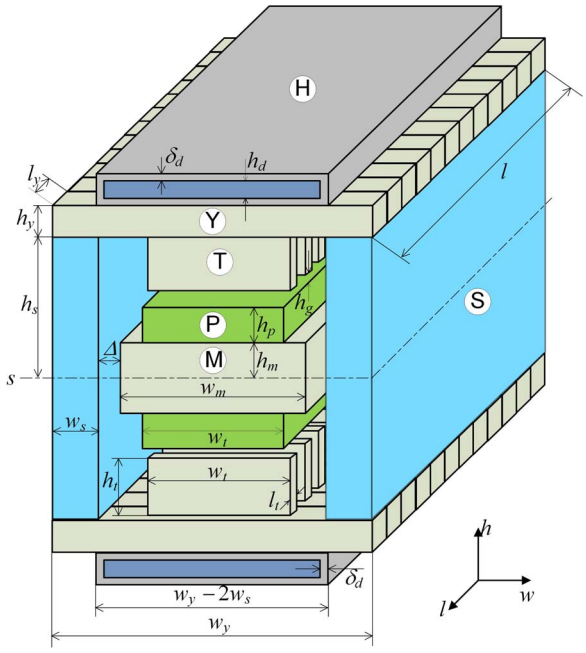

Fig. 4. PMSLM schematic 3-D representation with some characteristic dimensions (coils and front plate omitted).

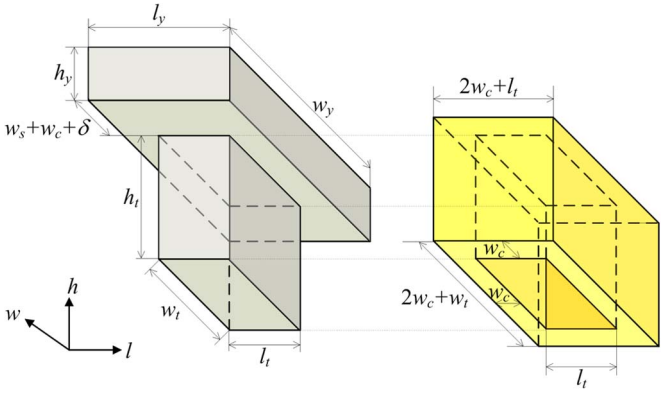

Fig. 5. Schematic view and dimensions of PMSLM yoke-tooth assembly and tooth coil.

w (width), and component dimensions are named accordingly. In Fig. 4, the cooling system (H) is included too, consisting of two water cold plates, fixed on the top and bottom actuator faces by thermal-conductive adhesive paste. For subsequent modeling purposes, permanent magnets and their aluminum retention boxes are modeled as a continuous layer (see Fig. 4), whose thermal conductivity and capacity will be, however, computed keeping into account both permanent magnet and aluminum box thermal properties. Fig. 5 shows a single tooth with relevant joke segment and wound coil. The characteristic dimensions shown in Figs. 4 and 5 are numerically provided in Table I, while significant motor ratings and performance data are provided in Table II.

From the data given in the table, in particular, one can observe that the motor is designed to operate at a very low speed (lower than 10 cm/s), which results in very low frequency (well below 1 Hz). This implies that stator and rotor core heating due to magnetic losses can be practically neglected (as experimentally proved through prototype tests). Moreover,

TABLE I
PMSLM CHARACTERISTIC DIMENSIONS (IN MILLIMETERS)

l	976.8	w_y	479.6	w_c	26.4	h_m	15	h_t	77	h_d	10
l_y	81.4	w_t	150	w_m	189.6	h_s	122	Δ	8	h_g	1.5
l_t	77	w_s	137	h_p	27	h_y	29	δ_d	2	δ	2.8

TABLE II
PMSLM RATINGS AND PERFORMANCE DATA

Maximum force	34300 N
Maximum speed	0.1 m/s
Maximum frequency	0.5 Hz
Maximum current *	20 A
Rated current *	5 A
Rated voltage *	400 V
Phase resistance *	24.2 Ω

* In case of series connection of all the coils of each phase

no significant heating due to friction losses or actuator motion occurs. In practice, the only source of heating to be considered is constituted by Joule losses in the stator coils.

III. PMSLM MODELING FOR THERMAL ANALYSIS

Compared to the design of a conventional rotating machine, a low-speed PMSLM architecture undoubtedly allows for some important simplifications that reduce thermal modeling and analysis efforts owing to the absence of moving parts and to the water cooling system [16]–[20]. On the other side, the noticeable compactness of the machine (with components placed in contact or at close distance from one another) leads to important heat transfers in all the directions l, w, h (see Figs. 4 and 5); hence, the motor thermal model needs to be a 3-D one with no possibility to simplify the problem into a 2-D one as sometimes done with rotating electric machines [18] as a first-attempt approach.

A. Simplifying Hypotheses

In order to model the PMSLM with a 3-D lumped-parameter strategy, it is essential to minimize the model extension in order to obtain fast simulation times. In view of this result, the following hypotheses are introduced.

a) The heat exchange occurs exactly in the same way in both the top and bottom halves of the actuator.
b) End effects in the axial direction (i.e., along the l direction, as shown in Fig. 4) can be neglected; equivalently, the actuator is supposed to have an infinite extension along the l direction.
c) The cooling fluid (water) flowing through the cold plate is assumed to have a uniform temperature T_F.
d) Due to the very low linear speeds, the mover translation does not contribute to the heat transfer process; motion effects are thus conservatively neglected.

The hypothesis a) is not rigorously exact because the heat transfer by natural convection from a heated (or cooled) plate is different depending on whether the plate faces upward or downward [17]. However, the heat transfer by natural convection is small compared to water cooling (see Section VI), so if an equal

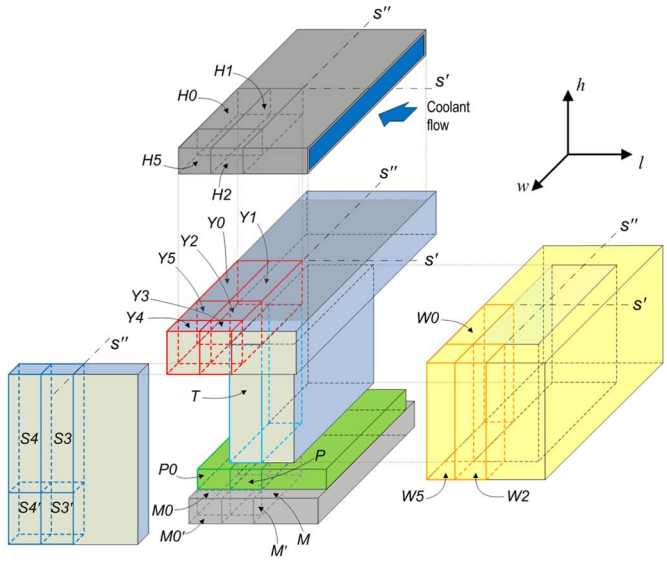

Fig. 6. Three-dimensional view of actuator blocks considered for thermal modeling based on symmetry considerations.

water flow occurs in both cold plates (see Fig. 4), hypothesis a) appears well founded.

As concerns hypothesis b), it would solidly hold for a full-scale actuator (much longer than the laboratory machine, as shown in Fig. 1). Testing results, however, proved (see Section VI-A) that the hypothesis does not lead to important errors even in the case of the reduced-scale prototype whose length is not significantly greater than its width (see Table I). As to hypothesis c), it will be also confirmed by water temperature measurements (see Section VI-A) taken at the cold plate inlet and outlet. However, such hypothesis is not claimed to be general and may not hold for longer actuators characterized by larger temperature rises between water inlet and outlet sections.

B. Exploiting Symmetry for Model Complexity Reduction

The hypothesis a) mentioned earlier enables one to identify the horizontal plane passing through line s (see Fig. 4) as a symmetry plane not only from a geometric viewpoint but also in terms of heat flows. As a consequence, for thermal analysis, it is sufficient to consider only one half of the machine, e.g., the top one placed above s, since no heat flow can occur across s. For the same reason, if we neglect end effects due to the finite actuator length along the l direction according to hypothesis b), we can assume that no heat transfer occurs from one tooth to the adjacent ones. We can therefore focus our attention on the actuator portion corresponding to a single would tooth as shown in Fig. 6. In such a reduced model, lines s' and s'' can be easily recognized from Fig. 6 as further symmetry planes which act as thermally insulated surfaces since no heat can flow across them.

As a result, the actuator portion to be modeled for thermal analysis reduces to the set of parallelepiped-shaped block volumes tagged in Fig. 6 with letters: T (tooth); $H0, H1, H2, H5$ (cold plate); $Y1, Y2, Y3, Y4, Y5, Y5$ (yoke); $P, P0$ (permanent magnet); $M, M0, M', M0'$ (mover); $S3, S4, S3', S4'$ (side shield); and $W0, W2, W5$ (tooth coil). The subdivision is such that the heat flow from one block to another occurs in

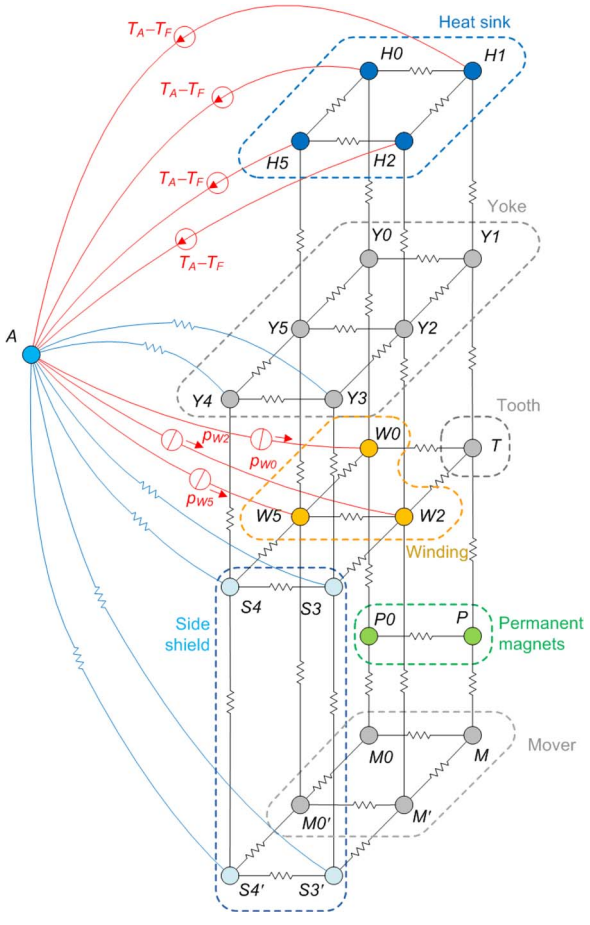

Fig. 7. Three-dimensional thermal network including heat sink nodes.

one of the three directions l, w, h only and through a rectangular cross section of uniform area, which simplify the computation of thermal conductances as explained next.

IV. Actuator Equivalent Thermal Network

A. Thermal Network Topology Definition

Once the actuator portion considered for thermal analysis has been subdivided into elementary parallelepiped-shaped blocks (see Fig. 6), the central point of each block is taken as a node of a thermal network as shown in Fig. 7. The network includes 24 nodes in addition to the "reference node" A which represents the air surrounding the actuator, assumed to be at a given temperature T_A. According to the well-known electrical–thermal analogy [18], the thermal network can be treated as an electrical one where the voltage of a node represents its temperature with respect to the air, the current between two nodes represents the heat flow flowing between them, a current-source generator connected between a node and the air (reference) represents the heating power developed in the node, voltage-source generators between two nodes represent a fixed temperature difference between them, and the electric conductance between two nodes represents the thermal conductance between them.

According to hypothesis c) mentioned in the previous section, heat sink nodes are supposed at a fixed water temperature T_F, which justifies the voltage generators connecting them to

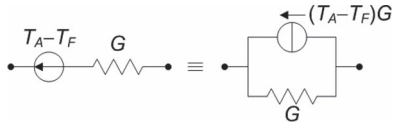

Fig. 8. Equivalent representation for a voltage generator connected in series with a conductance.

the air node at temperature T_A. As regards the heating power, given the negligible amount of core losses, it occurs only in the winding, as shown by the three current-source generators connected to coil nodes $(W0, W2, W5)$. Finally, concerning thermal power flows, straight-line connections are conventionally used in Fig. 7 to denote heat transfers by conduction, and curved light-blue connections are used to denote heat transfers by natural convection. The latter can be seen to occur from all end-shield nodes and from yoke nodes $Y3, Y4$ not covered by the cold plate (see Fig. 6).

Since heat sink nodes $H0, H1, H2, H5$ are assumed at equal temperature T_F, no heat transfer occurs among them, and their mutual conductance connections can be removed. Consequently, four voltage generators $(T_A - T_F)$ are connected in series with conductances $G_{H0,Y0}, G_{H1,Y1}, G_{H2,Y2}, G_{H5,Y5}$. Now, using the well-known circuit equivalence illustrated in Fig. 8, the network can be redrawn in a new form where only current-source generators are present and where the node count is reduced to 20 ($H0, H1, H2, H5$ disappear). The problem is then to compute the elements of the resulting thermal network, which can be done as explained in the following section.

B. Thermal Network Parameter Computation

1) Natural-Convection Conductances: Heat transfer by natural convection is considered from the side shields and from the yoke elements $Y3, Y4$ not covered by the cool plate. Side shields are treated as heated vertical plates, for which the natural-convection coefficient h_{vert} is defined as

$$h_{\text{vert}} = \frac{Nu_{\text{vert}}\, k}{(2h_s)} \tag{1}$$

where k is the air thermal conductivity, Nu_{vert} is the Nusselt number [17], and $2h_s$ is the side shield height (see Fig. 4). For the natural convection from a vertical plate in case of laminar flow, the Nusselt number can be computed as [22]

$$Nu_{\text{vert}} = 0.68 + 0.67\, Re_{\text{vert}}^{\frac{1}{4}} \Bigg/ \left[1 + \left(\frac{0.492}{Pr}\right)^{\frac{9}{16}}\right]^{\frac{4}{9}} \tag{2}$$

with Pr being the Prandtl number and Re_{vert} being the Rayleigh number of the air

$$Re_{\text{vert}} = \frac{9.81\beta\, \Delta T\, (2h_s)^3\, Pr}{\nu^2} \tag{3}$$

where β is the air coefficient of thermal expansion, v is the air dynamic viscosity, and ΔT is the difference between side shield and air temperatures. Once an average value is computed

for h_{vert}, the thermal conductance between side shield blocks $S3, S4, S3', S4'$ can be estimated. For example, the conductance between $S4$ and the air is [22]

$$G_{S4,A} = h_{\text{vert}} h_t w_c. \tag{4}$$

To compute the thermal conductance between nodes $Y3, Y4$ and the air, the yoke region (of area $w_s \times l$) not covered by the cold plate (see Fig. 4) is considered. It is regarded as a horizontal heated plate for which the Nusselt number can be estimated as [23]

$$Nu_{hor} = \begin{cases} 0.54\, Ra_{hor}^{\frac{1}{4}} & \text{if } 2\times 10^4 < Ra_{hor} < 10^6 \\ 0.15\, Ra_{hor}^{\frac{1}{3}} & \text{if } 10^6 < Ra_{hor} < 10^{11}. \end{cases} \tag{5}$$

In (5), Rayleigh number Ra_{hor} is

$$Ra_{hor} = \frac{9.81\beta\, \Delta T\, L^3 Pr}{\nu^2} \tag{6}$$

where L is the characteristic plate dimensions computed as

$$L = \frac{w_s l}{[2(w_s + l)]} \tag{7}$$

and ΔT is the temperature difference between the yoke surface under consideration and the air. The estimation of Nu_{hor} leads to compute the following convection coefficient and, hence, the conductances $G_{Y3,A}$ and $G_{Y4,A}$

$$h_{hor} = \frac{Nu_{hor}\, k}{L}. \tag{8}$$

2) Forced-Convection Conductances: The heat transfer from the actuator yoke segment to the cold plate mainly occurs by forced convection and, to a smaller extent, by conduction. For instance, the overall conductance between blocks $H1$ and $Y1$ can be computed as

$$G_{H1,Y1} = \left[\left(G^{cond}_{H1,Y1}\right)^{-1} + \left(G^{conv}_{H1,Y1}\right)^{-1} \right]^{-1} \tag{9}$$

with $G^{cond}_{H1,Y1}$, $G^{conv}_{H1,Y1}$ (respectively accounting for thermal conduction and forced convection) computed as [22]

$$G^{cond}_{H1,Y1} = \frac{k_{Fe} \left(\frac{l_t}{2}\right) \left(\frac{w_t}{2}\right)}{\left(\frac{h_t}{2}\right)} \tag{10}$$

$$G^{conv}_{H1,Y1} = h_w \left(\frac{l_t}{2}\right) \left(\frac{w_t}{2}\right) \tag{11}$$

where k_{Fe} is the steel thermal conductivity and h_w is the heat transfer coefficient by forced convection through the cold plate. This can be expressed as

$$h_w = \frac{Nu_w k_w}{D} \tag{12}$$

with k_w being the water thermal conductivity, Nu_w being the Nusselt number associated to the convection process, and D being the hydraulic diameter of the cold plate, defined as [17]

$$D = \frac{4\,(w_y - 2w_s)\, h_d}{[2(w_y - 2w_s + h_d)]}. \tag{13}$$

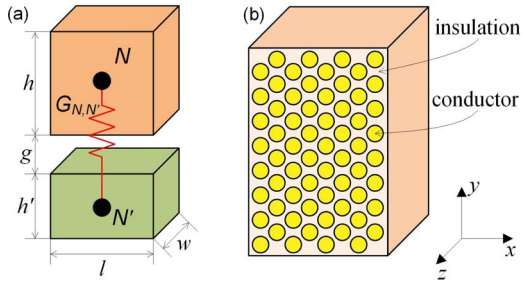

Fig. 9. (a) Scheme of two generic blocks separated by an air gap of width g. (b) Coil portion in a suitable x, y, z reference system.

For Nusselt number Nu_w, the following expression, derived from [17] and holding for laminar flow, is employed

$$Nu_w = 7.49 - 17.02\frac{h_d}{w_y - 2w_s} + 22.43\left(\frac{h_d}{w_y - 2w_s}\right)^2 - 9.94\left(\frac{h_d}{w_y - 2w_s}\right)^3 + \frac{0.065\left(\frac{D}{l}\right) Re_w\, Pr_w}{1 + 0.04\left[\left(\frac{D}{l}\right) Re_w\, Pr_w\right]^{\frac{2}{3}}} \tag{14}$$

where l is the axial actuator width (see Fig. 4), Pr_w is the water Prandtl number, and

$$Re_w = \frac{\rho_w\, V\, D}{\mu_w} \tag{15}$$

is the Reynolds number. In (15), ρ_w is the water density, μ_w is the water dynamic viscosity, and V is the water speed along the cold plate, associated with the flow rate Q

$$Q = V\,(w_y - 2w_s)\, h_d. \tag{16}$$

3) Thermal-Conduction-Related Conductances: Given two generic blocks, associated to thermal network nodes N, N' and separated by an air gap g as shown in Fig. 9(a), their mutual thermal conductance $G_{N,N'}$ is simply computed as

$$G_{N,N'} = \left[\left(k_N \frac{lw}{\frac{h}{2}}\right)^{-1} + \left(k_a \frac{lw}{g}\right)^{-1} + \left(k_{N'} \frac{lw}{\frac{h'}{2}}\right)^{-1} \right]^{-1} \tag{17}$$

where k_a, k_N, k'_N respectively denote the thermal conductivities of the air and of blocks N and N'.

Attention needs be paid to the thermal conductivity evaluation of coil blocks $W0, W2, W5$ which are nonisotropic. In fact, considering a coil portion as shown in Fig. 9(b), it conducts differently along directions x, y, z. Along z, copper conductors and insulation act as parallel paths for heat transfer; hence, the thermal conductivity k_z along z is

$$k_z = k_{Cu} k_{fill} + k_{ins}\,(1 - k_{fill}) \tag{18}$$

where k_{Cu}, k_{ins} are copper and insulation thermal conductivities and k_{fill} is the coil fill factor, defined as the copper to total xy cross section [see Fig. 9(b)]. Along the x and y directions, the thermal conductivity is nearly the same and depends on conductor geometry and on the fill factor. For example, in case of round wires with 1.5-mm diameter and a fill factor $k_{fill} = 0.59$, a 2-D thermal FEA leads to estimate thermal conductivity in the x and y directions as $k_x = k_y = 1.2$ W m^{-1}K^{-1}.

4) Equivalent Current Generator Elements: The heating power p_{Wi} injected into coil nodes Wi, with $i \in \{0, 2, 5\}$ (see Fig. 7) is computed as

$$p_{Wi} = \rho_{Cu}\sigma^2 V_{Wi} k_{fill} \tag{19}$$

where ρ_{Cu} is the copper electrical resistivity, σ is the current density, and V_{Wj} is the volume of the coil block Wi.

5) Thermal Capacitances: The thermal network defined in the form shown in Fig. 7, with conductance and current generator elements only, is useful for thermal analysis in the steady state under the hypothesis of constant heating sources [22]. For transient thermal analysis, the network needs to be enhanced by adding an equivalent capacitor between each node and the reference node A [18]. The value to be assigned to the capacitor C_N between node N and A equals the thermal capacitance of block N. Given the parallelepiped shape chosen for each block [see Fig. 9(a)], its thermal capacitance can be easily computed as

$$C_N = c_N \gamma_N \left(l \times w \times h\right) \tag{20}$$

where c_N, γ_N are the specific heat capacity and density of the node and l, w, h are node block dimensions.

V. Thermal Network Analytical Solution

Once the thermal network has been defined in its topology and constituting elements, it needs to be solved to find how actuator node temperatures evolve for a given heating source profile over time. This task is usually performed by the numerical integration of the differential equations associated to the thermal network model over a discretized time domain [18]. Such a procedure may be computationally heavy, particularly for a high number of nodes, due to the need for large matrix inverse computation at each integration step. The computational burden becomes particularly significant considering that, for a relatively large actuator size (like in the case under study), the thermal time constant can be on the order of hours: This means that, to obtain temperature waveforms in steady-state conditions under a given load cycle, time-consuming simulations over very long time frames need to be run. Such difficulties make thermal network solution through direct numerical computation little suitable when the thermal analysis is a part of a genetic-algorithm design optimization process [10], where hundreds or thousands of simulations are to be automatically performed in the search for a design optimum.

To cope with the problem, in this section, the thermal network presented in Section IV is mapped into a system of differential equations, for whose computationally efficient solution analytical techniques are derived exploiting matrix algebra techniques. The thermal analyses respectively during a stepwise load transient and during steady-state intermittent-load operation are addressed in sequence.

A. Analytical Solution for Load Transient Study

The equivalent thermal network of the actuator described in Section IV can be solved using the voltage-node method known from electric circuit theory [24]. For this purpose, calling Z the number of physical model nodes, we shall introduce the Z-sized vectors $\boldsymbol{\theta}$ and $\mathbf{p}$ defined as

$$\boldsymbol{\theta} = \left(\theta_1\ \theta_2\ \theta_3\ \cdots\ \theta_Z\right)^t, \mathbf{p}0 - \left(p_1\ p_2\ p_3\ \cdots\ p_Z\right)^t \tag{21}$$

where θ_j is the difference between the temperature of node j and the air temperature T_A ($\theta_j = T_j - T_A$) and p_j is the heating power that originates in node j. Thus, the application of the node voltage method [24] combined with the electrothermal analogy [18] leads to write the following matrix differential equation:

$$\mathbf{p} = \mathbf{G}\boldsymbol{\theta} - \mathbf{C}\left(\frac{d\boldsymbol{\theta}}{dt}\right) \tag{22}$$

where $\mathbf{G}, \mathbf{C}$ are the thermal conductance and capacitance matrices defined as per (23) and (24), shown at the bottom of the page, with $G_{i,j}$ indicating the thermal conductance between nodes i and j and G_i being the thermal conductance between node i and the air.

Introducing the Laplace transforms of vectors $\boldsymbol{\theta}$ and $\mathbf{p}$

$$\Theta(s) = \mathcal{L}\left\{\boldsymbol{\theta}(t)\right\}, \mathbf{P}(s) = \mathcal{L}\left\{\mathbf{p}(t)\right\} \tag{25}$$

(22) can be written as (26), leading to

$$\mathbf{P}(s) = \mathbf{G}\Theta(s) - s\mathbf{C}\Theta(s) = (\mathbf{G} - s\,\mathbf{C})\Theta(s) \tag{26}$$

$$\Theta(s) = (\mathbf{G} - s\mathbf{C})^{-1}\mathbf{P}(s) = \mathbf{Y}(s)^{-1}\mathbf{P}(s) \tag{27}$$

where the thermal admittance matrix is defined as

$$\mathbf{Y}(s) = \mathbf{G} - s\mathbf{C} = -\mathbf{C}\left(s\mathbf{I} - \mathbf{C}^{-1}\mathbf{G}\right). \tag{28}$$

$$\mathbf{C} = \begin{pmatrix} C_1 & 0 & \cdots & 0 \\ 0 & C_2 & \cdots & 0 \\ \vdots & \vdots & \ddots & \vdots \\ 0 & 0 & \cdots & C_Z \end{pmatrix} \tag{23}$$

$$\mathbf{G} = \begin{pmatrix} -G_1 - \sum_{j\neq 1} G_{1,j} & G_{1,2} & \cdots & G_{1,Z} \\ G_{1,2} & -G_2 - \sum_{j\neq 2} G_{2,j} & \cdots & G_{2,Z} \\ \vdots & \vdots & \ddots & \vdots \\ G_{1,Z} & G_{2,Z} & \cdots & -G_Z - \sum_{j\neq Z} G_{Z,j} \end{pmatrix} \tag{24}$$

The temperature vector evolution over time can be thereby obtained by inverse Laplace transform as

$$\boldsymbol{\theta}(t) = \mathcal{L}^{-1}\left\{\Theta(s)\right\} = \mathcal{L}^{-1}\left\{\mathbf{Y}(s)^{-1}\mathbf{P}(s)\right\}. \tag{29}$$

Particularly in case of a large number of nodes, the computation of $\mathbf{Y}(s)^{-1}$ might be troublesome, requiring the inverse of a $Z \times Z$ matrix to be found symbolically. To simplify calculations, we introduce the eigendecomposition of matrix $\mathbf{C}^{-1}\mathbf{G}$ which appears in (28) as

$$\mathbf{C}^{-1}\mathbf{G} = \mathbf{T}\,\Lambda\mathbf{T}^{-1} \tag{30}$$

where $\mathbf{\Lambda}$ is the diagonal matrix (31), λ_j denotes the eigenvalues of $\mathbf{C}^{-1}\mathbf{G}$ $(1 \leq j \leq Z)$, and the jth column of $\mathbf{T}$ is the eigenvector of $\mathbf{C}^{-1}\mathbf{G}$ associated to eigenvalue λ_j

$$\Lambda = \begin{pmatrix} \lambda_1 & 0 & \cdots & 0 \\ 0 & \lambda_2 & \cdots & 0 \\ \vdots & \vdots & \ddots & \vdots \\ 0 & 0 & \cdots & \lambda_Z \end{pmatrix}. \tag{31}$$

We can observe that the eigendecomposition of $\mathbf{C}^{-1}\mathbf{G}$ as per (30) is certainly possible with λ_j being real numbers because $\mathbf{C}^{-1}\mathbf{G}$ is a symmetrical real-valued matrix, which assures that it can be diagonalized and has real eigenvalues [25]. A variety of algorithms, like the Jacobi method, can be used to easily diagonalize a real symmetric matrix [25].

The substitution of (30) into (28) yields

$$\mathbf{Y}(s)^{-1} = -\mathbf{T}\left(s\mathbf{I} - \Lambda\right)^{-1}\mathbf{T}^{-1}\mathbf{C}^{-1} \tag{32}$$

where $(s\mathbf{I} - \Lambda)^{-1}$ is a diagonal matrix whose diagonal elements are $1/(s - \lambda_j)$, with $j = 1 \ldots Z$.

As a particular case, one can be interested in studying the thermal response to a step change in the thermal load vector $\mathbf{p}(t)$, e.g., to see the temperatures rise after a start up with a given constant thermal load vector $\mathbf{p}_0$. In this case, we have $\mathbf{P}(s) = \mathcal{L}\{\mathbf{p}(t)\} = \mathbf{p}_0/s$ and (29), and (32) gives

$$\boldsymbol{\theta}(t) = -\mathbf{T}\mathcal{L}^{-1}\left\{\frac{(s\mathbf{I} - \Lambda)^{-1}}{s}\right\}\mathbf{T}^{-1}\mathbf{C}^{-1}\mathbf{p}_0 \tag{33}$$

$$\mathcal{L}^{-1}\left\{\frac{(s\mathbf{I} - \Lambda)^{-1}}{s}\right\} = \begin{pmatrix} -\frac{h(t)}{\lambda_1} + \frac{e^{\lambda_1 t}}{\lambda_1} & 0 & \cdots & 0 \\ 0 & -\frac{h(t)}{\lambda_2} + \frac{e^{\lambda_2 t}}{\lambda_2} & \cdots & 0 \\ \vdots & \vdots & \ddots & \vdots \\ 0 & 0 & \cdots & -\frac{h(t)}{\lambda_Z} + \frac{e^{\lambda_Z t}}{\lambda_Z} \end{pmatrix} \tag{34}$$

where $h(t)$ indicates the Heaviside step function [25]. Equations (33) and (34) are a closed-form expression of the temperature response to a step change $\mathbf{p}_0$ in the heating load vector.

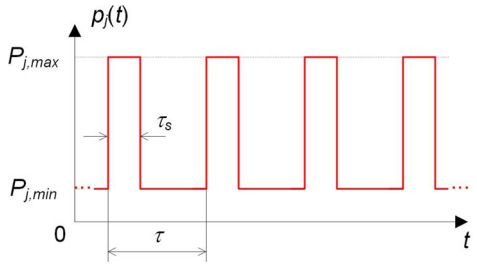

Fig. 10. Steady-state profile of the heating power p_j at node j.

B. Analytical Solution for Intermittent-Load Operation

Another typical point worth being investigated is how the actuator thermally behaves, at steady state, for intermittent-load operation, i.e., when subject to a given periodic load cycle. In these conditions, the heating power p_j in the generic node j [hence the jth element of vector $-\mathbf{p}$] is supposed to have a periodic profile as shown in Fig. 10, oscillating between a maximum $P_{j,\max}$ and a minimum $P_{j,\min}$ with period τ. It should be noted that a unique heating power waveform is used for all the nodes; hence, only the adaptation of the parameters $P_{j,\max}P_{j,\min}$ for any given jth is needed, as explained in the following.

For network nodes associated to coil subblocks like $W0$ (see Fig. 6), the heating power is computed as per (19), so

$$P_{j,\min} \propto \sigma_{\min}^2,\ P_{j,\max} \propto \sigma_{\max}^2 \tag{35}$$

where $\sigma_{\min}$ and $\sigma_{\max}$ are the minimum and maximum current densities in the coils.

Some network nodes are connected to the reference node A by equivalent constant current generators. For such nodes, the rectangular-wave diagram shown in Fig. 10 applies as well, by simply imposing that $P_{j,\max} = P_{j,\min}$ equals the constant power source associated to the nodes. Finally, for a generic node j which is not connected to any equivalent current generator, we can simply set $P_{j,\max} = P_{j,\min} = 0$.

With the mentioned clarifications and by means of complex Fourier series, we can write for the generic node j

$$p_j(t) = \sum_{k=-\infty}^{+\infty} c_{k,j}e^{i\omega kt} \tag{36}$$

where $\omega = 2\pi/\tau$, i is the imaginary unit, and

$$c_{k,j} = \begin{cases} P_{j,\max}\left(\frac{\tau_s}{\tau}\right) + P_{j,\max}\left[\frac{(\tau-\tau_s)}{\tau}\right], & \text{if } k = 0 \\ \left[(P_{j,\max} - P_{j,\min})\sin\left(\frac{\omega\tau_s k}{2}\right)\right]/\pi k, & \text{if } k \neq 0 \end{cases}. \tag{37}$$

Therefore, in vector terms, $\mathbf{p}$ in (21) becomes

$$\mathbf{p}(t) = -\sum_{k=-\infty}^{+\infty} \mathbf{c}_k e^{i\omega kt} \tag{38}$$

where $\mathbf{c}_k$ is the Z-sized vector whose jth element is (37).

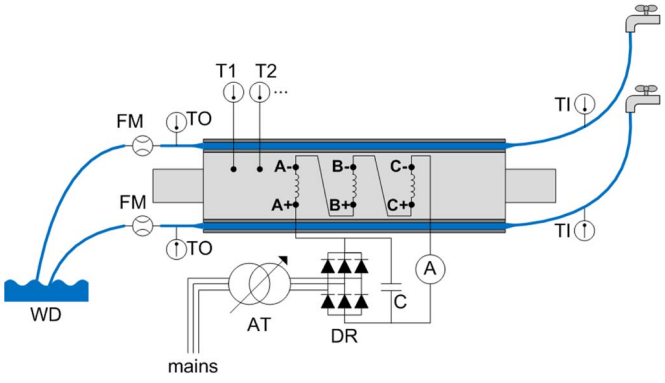

Fig. 11. Test layout for heat-run tests.

The steady-state response of the thermal system described by the differential (22), when subject to the power vector (38), can be easily found by the superposition principle [25] as

$$\boldsymbol{\theta}(t) = -\sum_{k=-\infty}^{+\infty} \left(\mathbf{G} - ik\omega\mathbf{C}\right)^{-1} \mathbf{c}_k e^{i\omega kt}$$

$$= -\sum_{k=-\infty}^{+\infty} \mathbf{Y}(ik\omega)^{-1} \mathbf{c}_k e^{i\omega kt} \quad (39)$$

or equivalently, using decomposition (32) for $\mathbf{Y}^{-1}$

$$\boldsymbol{\theta}(t) = \mathbf{T} \sum_{k=-\infty}^{+\infty} \left(ik\omega\mathbf{I} - \Lambda\right)^{-1} \mathbf{T}^{-1}\mathbf{C}^{-1}\mathbf{c}_k e^{i\omega kt} \quad (40)$$

where $(ik\omega\mathbf{I} - \Lambda)^{-1}$ is the diagonal matrix whose diagonal elements are $1/(ik\omega - \lambda_1)$ for $j = 1 \dots Z$.

Equation (40) directly gives the steady-state actuator temperatures for intermittent-load operation as a Fourier series expansion with no need for either matrix inverse computation or time-domain discretization algorithms.

VI. Experimental Validations Through Prototype Thermal Testing

The model developed for PMSLM thermal analysis (see Section IV) and the analytical methods for its solution (see Section V) are herein validated by some thermal tests on the PMSLM laboratory prototype shown in Fig. 1 equipped with a suitable cooling system based on cold plates.

The basic layout used for testing is shown in Fig. 11, with thermal detectors T1, T2, ... placed in the actuator as sketched in Fig. 12. The physical test layout, including the water cold plates used for PMSLM cooling, is represented in Fig. 13. The three actuator phases are series connected and supplied via a dc source obtained directly by the mains through an autotransformer (AT) and a diode rectifier (DR), which is shunt connected to a capacitor C used to smooth the ripple of the supply voltage. The use of such a connection is chosen to obtain an overall null air-gap force on the slider, which is thus maintained at standstill with no need for locking it. Furthermore, the series connection guarantees that all coils are heated by the same dc current, whose amplitude is monitored

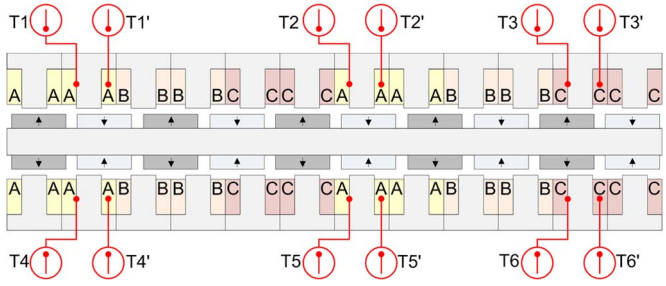

Fig. 12. Location of embedded thermal detectors.

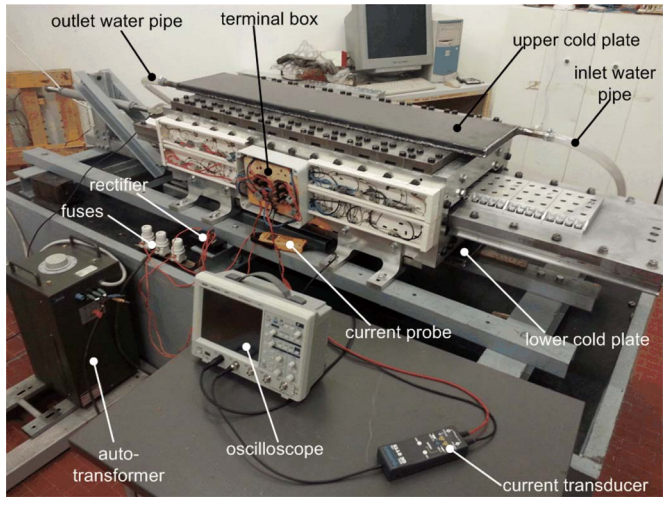

Fig. 13. Physical layout used for thermal tests.

through an amperometer (A). Cold plates are fed by cool water, whose temperatures are measured at inlet and outlet sections by thermal detectors (TI) and (TO), respectively. Flow rates through the two cold plates are also measured by dedicated flow meters (FM). This enables to adjust the water supply system so as to maintain the flow rate and temperature equal and constant in both cold plates as much as possible. To avoid water heating during the test, an open-loop cooling configuration is adopted that conveys the water exiting cold plates into a water discharge (WD). Finally, actuator temperatures are measured by means of the 12 thermal detectors (of "Pt100" type) located as shown in Fig. 12: Detectors $T1 \dots T6$ are embedded inside the coils (approximately in the center of the straight coil side), while detectors $T1' \dots T6'$ are placed between such coil sides and the teeth (see Fig. 2). A thermal detector is also placed in the center of the side shield external surface (see Fig. 1).

A. Heat-Run Test

The first test aims at validating the transient thermal model presented in Section V-A by means of a heat-run test. Starting from a rest condition where the actuator is in thermal balance with the environment, a current load is applied in a stepwise manner and maintained constant for hours. The load is fixed so as to have a constant current density $\sigma = 4$ A/mm^2 in the PMSLM conductors, i.e., supplying the phases with a dc current of 7 A through the circuit shown in Fig. 11. During the test,

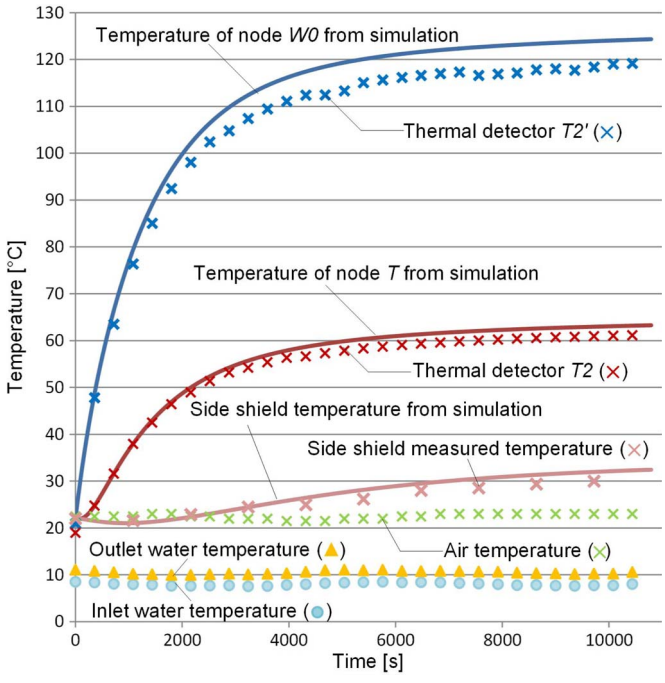

Fig. 14. Temperature rise test result compared to thermal simulation outputs (solid lines).

TABLE III
COMPARISON OF TEMPERATURE READINGS (°C) FROM DIFFERENT EMBEDDED DETECTORS AT STEADY STATE

Thermal detector	Analytical result	Steady-state reading	Thermal detector	Analytical result	Steady-state reading
T1'	124.6	116.4	T4'	124.6	117.1
T2'	124.6	119.3	T5'	124.6	120.1
T3'	124.6	115.9	T6'	124.6	116.7
T1	64.5	57.4	T4	64.5	58.4
T2	64.5	60.2	T5	64.5	60.6
T3	64.5	57.3	T6	64.5	56.8

temperature measurements are taken for the air (in a point placed approximately 2 m from the actuator), for the water at cold plate inlet and outlet sections, and from the thermal detectors embedded in the actuator (see Fig. 12). In Fig. 14, test results are shown and compared to thermal simulation outputs obtained from (33) and (34). For simulations, an average air temperature $T_A = 22$ °C, an average cold plate water temperature $T_F = 9.3$ °C, and a constant water flow of 0.2 L/s per cold plate (obtained from measurements) are assumed.

The comparison between measured temperatures and analytical predictions is shown in Fig. 14 for the inner part of actuator coils (node $W0$ in Fig. 6) and teeth (node T in Fig. 6). $W0$ and T are chosen as the points where the maximum temperatures occur in the machine winding and core, respectively. Moreover, measurements from the embedded detectors $T2'$ and $T2$, placed at the actuator center (see Fig. 12) and from the detectors located on the side shields, are displayed in Fig. 14. It can be seen how temperature readings are in good accordance with simulation results. As concerns the other thermal detectors, their temperature diagrams are not included in Fig. 14, but only steady-state readings are provided in Table III.

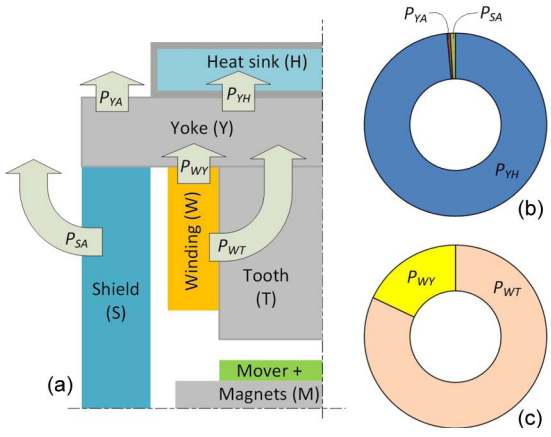

Fig. 15. Graphical representation of the main heat flows occurring in the machine at steady state based on thermal model solution.

The values shown in Table III confirm that the temperatures are uniformly distributed along the axial direction: Due to end effects, coils placed at actuator ends are slightly cooler than central ones, but with temperature discrepancies below 6%. The hypothesis of thermal symmetry with respect to the mover is also well confirmed.

Regarding the adoption of a dc supply system during the test, this actually imposes the same thermal load on the machine as in the case when it is supplied with a low-frequency balanced three-phase ac current system having an amplitude of 7 A rms. This has been experimentally checked by imposing a low frequency (1 Hz) ac supply giving null overall force and checking that results do not change with respect to those obtained in case of dc supply.

The model solution gives access to the main thermal flows taking place in the machine at steady state. In fact, once the solution is known in terms of node temperatures, the heat power $p_{NN'}$ flowing between two given adjacent nodes N, N' having steady-state temperatures T, T' is given by $p_{NN'} = (T - T')G_{NN'}$, where $G_{NN'}$ is the conductance between N and N'. The main paths along which heat flows through the actuator are shown in Fig. 15(a) together with some graphs [see Fig. 15(b) and (c)] illustrating the relative amounts of power transferred along the various paths. It can be seen that majority (P_{WT}, 82%) of the heat produced in the winding is transferred to the tooth and, from this, to the yoke, while a less amount of it (P_{WY}, 18%) is directly transferred to the yoke. Out of the total heat passing through the yoke, the vast majority of it (P_{YH}, 98.5%) goes into the water cold plate which acts as the principal heat sink, while only a very small percentage ($P_{SA} + P_{YA}$, 1.5%) is transferred to the air by natural convection from the side shield and the yoke portions not covered by cold plates.

Finally, the thermal simulation results shown in Fig. 14 are run assuming water and air temperatures of 9.3 °C and 22 °C, respectively, to reflect laboratory test conditions. The thermal model can be also used to reproduce more severe environmental conditions which may occur in machine operation after onboard installation. For example, Table IV compares the steady-state maximum temperatures predicted in machine winding and core (teeth) in laboratory test conditions and in a case when water and air temperatures are equal to 40 °C and 50 °C, respectively

TABLE IV
THERMAL SIMULATION RESULTS FOR DIFFERENT WATER AND AIR TEMPERATURES

	Maximum winding steady-state temperature		Maximum core steady-state temperature	
	Absolute T	ΔT over air	Absolute T	ΔT over air
Laboratory test conditions (T_A=22°C, T_W=9.3°C)	126 °C	104 K	65 °C	43 K
Worse environmental conditions (T_A=50°C, T_W=40°C)	156 °C	106 K	94 °C	44 K

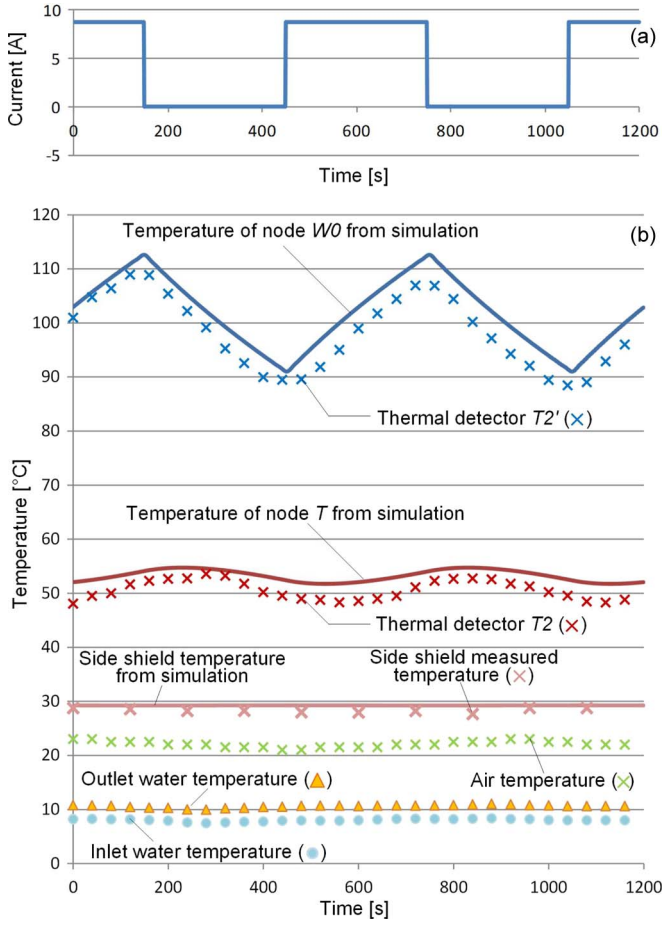

Fig. 16. Diagrams of (a) phase currents and (b) measured and simulated temperatures during steady-state intermittent-load operation.

(predicted results are shown in the table as measurements referring to laboratory tests are provided in Fig. 14 and Table III). It can be seen from the simulation results that, although the absolute temperatures in the two cases substantially change, the results in terms of temperature rise over the air do not significantly differ.

B. Intermittent-Load Steady-State Testing

The test presented in this section is intended to validate the actuator steady-state thermal modeling in the presence of a periodic load cycle (see Section V-B). The actuator is loaded with a 50% duty cycle according to the phase current diagram shown in Fig. 16(a). The loading is thereby periodic with period $\tau = 600$ s.

Over each period, the current is kept constant at a value of 8.8 A (corresponding to a current density of 5 A/mm^2) for a "service" interval $\tau_s = 300$ s, while in the rest of the period, the actuator is not supplied. The intermittent loading is applied for 3 h according to this pattern until the actuator reaches a steady-state condition. At this point, temperature measurements are taken as shown in Fig. 16(b). For simulations, an average air temperature $T_A = 21.8$ °C, an average cold plate water temperature $T_F = 9.1$ °C, and a water flow rate of 0.2 L/s are assumed.

Simulation outputs resulting from (40), with index k truncated so that it ranges between -30 and 30, are plotted in Fig. 16(b) focusing, in particular, on the temperatures of nodes $W0$ (coil), T (tooth), and $S3$ (end shield). As done for the transient heat-run test, the simulated temperatures of these nodes are compared to the readings of the corresponding thermal detectors, showing a satisfactory matching, in consideration that model thermal parameters have been determined from calculation and no tuning has been performed.

VII. CONCLUSION

PMLSMs are a very interesting solution for the direct-drive full-electric actuation of many loads traditionally driven by hydraulic machinery. This paper considers a PMSLM prototype designed to operate shipboard loads requiring high thrusts at very low speeds, such as rudders, stabilizing fins, and bow-thruster steering systems. A 3-D lumped-parameter thermal model of the actuator has been developed, exploiting all intrinsic machine symmetries so as to maximize the spatial density of nodes and, therefore, the accuracy of results. Furthermore, computationally efficient techniques have been proposed for analytically solving the model with no need for time discretization or troublesome large matrix inversions. The presented methodology has been experimentally assessed by comparison with thermal tests on the actuator prototype, both during a stepwise load change and in case of intermittent-load operation according to a defined service cycle. The comparison between analytical results and measurements has highlighted a satisfactory accuracy for the proposed method and has basically confirmed some simplifying hypotheses underlying it, such as the nearly uniform temperature distribution along the thrust axis direction, the strong prevalence of forced convection through the water heat exchanger over natural convection, and the possibility to disregard core losses owing to the low supply frequency. Regarding the computational performance, it has been proved that it is possible to use the proposed methodology to run practically instantaneous thermal simulations based on simple analytical solution formulas instead of time-consuming finite-element analyses that typically require several hours to produce the same results. A further advantage of the modeling approach presented is that it does not require heuristic or test-based calibration. Such feature, however, closely relates to the characteristic of the actuator type taken into account, such as its very low speed and frequency which make it possible to disregard core losses as well as ventilation effects due to slider motion.

REFERENCES

[1] A. Boldea and S. Nasar, *Linear Motion Electromagnetic Devices*. New York, NY, USA: Taylor & Francis, 2001.

[2] N. Hodgins, O. Keysan, A. S. McDonald, and M. A. Mueller, "Design and testing of a linear generator for wave-energy applications," *IEEE Trans. Ind. Electron.*, vol. 59, no. 5, pp. 2094–2103, May 2012.

[3] M. Leijon *et al.*, "Multiphysics simulation of wave energy to electric energy conversion by permanent magnet linear generator," *IEEE Trans. Energy Convers.*, vol. 20, no. 1, pp. 219–224, Mar. 2005.

[4] R. Vermaak and M. J. Kamper, "Design aspects of a novel topology air-cored permanent magnet linear generator for direct drive wave energy converters," *IEEE Trans. Ind. Electron.*, vol. 59, no. 5, pp. 2104–2115, May 2012.

[5] J. Prudell, M. Stoddard, E. Amon, T. K. A. Brekken, and A. Von Jouanne, "A permanent-magnet tubular linear generator for ocean wave energy conversion," *IEEE Trans. Ind. Appl.*, vol. 46, no. 6, pp. 2392–2400, Nov./Dec. 2010.

[6] J. Wang, W. Wang, G. W. Jewell, and D. Howe, "A low-power, linear, permanent-magnet generator/energy storage system," *IEEE Trans. Ind. Electron.*, vol. 49, no. 3, pp. 640–648, Jun. 2002.

[7] L. N. Tutelea, M. C. Kim, M. Topor, J. Lee, and I. Boldea, "Linear permanent magnet oscillatory machine: Comprehensive modeling for transients with validation by experiments," *IEEE Trans. Ind. Electron.*, vol. 55, no. 2, pp. 492–500, Feb. 2008.

[8] Z. Z. Liu, F.-L. Luo, and M. A. Rahman, "Robust and precision motion control system of linear-motor direct drive for high-speed X-Y table positioning mechanism," *IEEE Trans. Ind. Electron.*, vol. 52, no. 5, pp. 1357–1363, Oct. 2005.

[9] C. Bruzzese, A. Tessarolo, T. Mazzuca, and G. Scala, "A closer look at conventional hydraulic ship actuator systems and the convenience of shifting to (possibly) all-electric drives," in *Proc. IEEE ESTS*, Arlington, VA, USA, Apr. 22–24, 2013, pp. 220–227.

[10] M. Bortolozzi *et al.*, "Magnetic optimization of a fault-tolerant linear permanent magnet modular actuator for shipboard applications," in *Proc. IEEE Int. SDEMPED*, Valencia, Spain, Aug. 27–30, 2013.

[11] C. Bruzzese, A. Tessarolo, T. Mazzuca, and G. Scala, "A high-thrust linear electric motor prototype for perspective replacement of ship-board hydraulic actuators," in *Proc. AEIT Annu. Conf.*, Mondello, Italy, Oct. 3–5, 2013, pp. 1–6.

[12] T. Minav *et al.*, "Electric energy recovery system for a hydraulic forklift—Theoretical and experimental evaluation," *IET Elect. Power Appl.*, vol. 5, no. 4, pp. 377–385, Apr. 2011.

[13] D. Sepasi, R. Nagamune, and F. Sassani, "Tracking control of flexible ball screw drives with runout effect and mass variation," *IEEE Trans. Ind. Electron.*, vol. 59, no. 2, pp. 1248–1256, Feb. 2012.

[14] X. Huang, L. Li, B. Zhou, C. Zhang, and Z. Zhang, "Temperature calculation for tubular linear motor by the combination of thermal circuit and temperature field method considering the linear motion of air-gap," *IEEE Trans. Ind. Electron.*, vol. 61, no. 8, pp. 3923–3931, Aug. 2014.

[15] I. Vese, F. Marignetti, and M. M. Radulescu, "Multiphysics approach to numerical modeling of a permanent-magnet tubular linear motor," *IEEE Trans. Ind. Electron.*, vol. 57, no. 1, pp. 320–326, Jan. 2010.

[16] A. Boglietti *et al.*, "Evolution and modern approaches for thermal analysis of electrical machines," *IEEE Trans. Ind. Electron.*, vol. 56, no. 3, pp. 871–882, Mar. 2009.

[17] D. A. Staton and A. Cavagnino, "Convection heat transfer and flow calculations suitable for electric machines thermal models," *IEEE Trans. Ind. Electron.*, vol. 55, no. 10, pp. 3509–3516, Oct. 2008.

[18] L. Alberti and N. Bianchi, "A coupled thermal-electromagnetic analysis for a rapid and accurate prediction of IM performance," *IEEE Trans. Ind. Electron.*, vol. 55, no. 10, pp. 3575–3582, Oct. 2008.

[19] G. Traxler-Samek, R. Zickermann, and A. Schwery, "Cooling airflow, losses, temperatures in large air-cooled synchronous machines," *IEEE Trans. Ind. Electron.*, vol. 57, no. 1, pp. 172–180, Jan. 2010.

[20] L. Weili, G. Chunwei, and Z. Ping, "Calculation of a complex 3-D model of a turbogenerator with end region regarding electrical losses, cooling, heating," *IEEE Trans. Energy Convers.*, vol. 26, no. 4, pp. 1073–1080, Dec. 2011.

[21] A. M. EL-Refaie, "Fractional-slot concentrated-windings synchronous permanent magnet machines: Opportunities and challenges," *IEEE Trans. Ind. Electron.*, vol. 57, no. 1, pp. 107–121, Jan. 2010.

[22] F. P. Incropera, D. P. Dewitt, T. Bergman, and A. S. Lavine, *Fundamentals of Heat and Mass Transfer*, 3rd ed. Hoboken, NJ, USA: Wiley, 1990, p. 543.

[23] J. R. Lloyd and W. R. Moran, "Natural convection adjacent to horizontal surface of various planforms," *J. Heat Transfer*, vol. 96, no. 4, pp. 443–447, Nov. 1974.

[24] J. W. Nilsson and S. A. Riedel, *Electric Circuits*, 9th ed. Upper Saddle River, NJ, USA: Prentice-Hall, 2011.

[25] A. Quarteroni, R. Sacco, and F. Saleri, *Numerical Mathematics*. New York, NY, USA: Springer-Verlag, 2000, pp. 183–240.

Alberto Tessarolo (M'06) received the Laurea degree in electrical engineering from the University of Trieste, Trieste, Italy, in 2000 and the Ph.D. degree in electrical engineering from the University of Padova, Padova, Italy, in 2011.

After some years' experience in the R&D department of NIDEC-ASI (formerly Ansaldo Sistemi Industriali) as a High-Power Motor and Generator Designer, he joined the University of Trieste in 2006, where he presently serves as an Assistant Professor and teaches the course on electric machine design. He leads several research projects in cooperation with international electric machine manufacturers and final users. His main research interests are in the area of electric machine modeling, analysis, and design optimization, a field in which he has authored around 100 international journal and conference papers.

Dr. Tessarolo is a member of various IEEE societies (Power and Energy Society, Industry Applications Society, Power Electronics Society, Industrial Electronics Society, Magnetics Society, and Reliability Society). He presently serves as an Editor for the IEEE TRANSACTIONS ON ENERGY CONVERSION. He is a Registered Professional Engineer in Italy.

Claudio Bruzzese (S'05–M'08) received the M.Sc. (*cum laude*) and Ph.D. degrees in electrical engineering from the University of Rome "La Sapienza," Rome, Italy, in 2002 and 2008, respectively.

He served as a designer of electrical power systems between 1998 and 2002. After graduation, he was with the National Power System Management Company. Since September 2002, he has been with the Department of Astronautical, Electrical, and Energy Engineering, University of Rome "La Sapienza," as an Assistant Researcher and, since 2011, as an Assistant Professor. He is a consultant for the Italian Ministry of Defense and has developed research projects for the Military Research National Program. He was a Visiting Researcher at the University of Victoria, Victoria, BC, Canada, in 2012. His research interests include the fault diagnosis of induction and synchronous machines, railway and naval power systems, linear drives, and electromechanical design and modeling. He is the author or coauthor of about 70 technical papers and is the holder of four patents.

Dr. Bruzzese is member of the IEEE Industrial Electronics Society. He is a Registered Professional Engineer in Italy.